

RESEARCH ARTICLE

10.1002/2016JA022812

Key Points:

- Modeling of ground-based radio wave observations with BARREL-specified electron precipitation fluxes at energies of ~ 1.0 – 1.2 MeV
- Two precipitation patches, with longitudinal dimensions of 1.5–3.5 h in MLT, are observed to drift westward passed the BARREL balloon
- A peaked spectrum is suggested, but improved instrumentation is required to unambiguously resolve form of the electron precipitation

Correspondence to:

M. A. Clilverd,
macl@bas.ac.uk

Citation:

Clilverd, M. A., C. J. Rodger, M. McCarthy, R. Millan, L. W. Blum, N. Cobbett, J. B. Brundell, D. Danskin, and A. J. Halford (2017), Investigating energetic electron precipitation through combining ground-based and balloon observations, *J. Geophys. Res. Space Physics*, 122, 534–546, doi:10.1002/2016JA022812.

Received 14 APR 2016

Accepted 3 JAN 2017

Accepted article online 7 JAN 2017

Published online 21 JAN 2017

Investigating energetic electron precipitation through combining ground-based and balloon observations

Mark A. Clilverd¹ , Craig J. Rodger² , Michael McCarthy³ , Robyn Millan⁴ , Lauren W. Blum⁵ , Neil Cobbett¹ , James B. Brundell² , Donald Danskin⁶ , and Alexa J. Halford⁴ 

¹British Antarctic Survey (NERC), Cambridge, UK, ²Department of Physics, University of Otago, Dunedin, New Zealand, ³Department of Earth and Space Sciences, University of Washington, Seattle, Washington, USA, ⁴Department of Physics and Astronomy, Dartmouth College, Hanover, New Hampshire, USA, ⁵Space Sciences Laboratory, University of California, Berkeley, California, USA, ⁶Geomagnetic Laboratory, Natural Resources Canada, Ottawa, Ontario, Canada

Abstract A detailed comparison is undertaken of the energetic electron spectra and fluxes of two precipitation events that were observed in 18/19 January 2013. A novel but powerful technique of combining simultaneous ground-based subionospheric radio wave data and riometer absorption measurements with X-ray fluxes from a Balloon Array for Relativistic Radiation-belt Electron Losses (BARREL) balloon is used for the first time as an example of the analysis procedure. The two precipitation events are observed by all three instruments, and the relative timing is used to provide information/insight into the spatial extent and evolution of the precipitation regions. The two regions were found to be moving westward with drift periods of 5–11 h and with longitudinal dimensions of $\sim 20^\circ$ and $\sim 70^\circ$ (1.5–3.5 h of magnetic local time). The electron precipitation spectra during the events can be best represented by a peaked energy spectrum, with the peak in flux occurring at ~ 1 – 1.2 MeV. This suggests that the radiation belt loss mechanism occurring is an energy-selective process, rather than one that precipitates the ambient trapped population. The motion, size, and energy spectra of the patches are consistent with electromagnetic ion cyclotron-induced electron precipitation driven by injected 10–100 keV protons. Radio wave modeling calculations applying the balloon-based fluxes were used for the first time and successfully reproduced the ground-based subionospheric radio wave and riometer observations, thus finding strong agreement between the observations and the BARREL measurements.

1. Introduction

Physical processes that occur in the radiation belts can result in the precipitation of energetic electrons into the atmosphere [Millan and Thorne, 2007; Thorne, 2010]. When energetic electrons are deposited into the atmosphere they provide a loss mechanism by which the radiation belts can become depleted, or at least reduced in flux. Electron precipitation is one of the processes by which poststorm radiation belt electron flux enhancements can relax back to their quiet time levels [Horne et al., 2009].

Wave-particle interactions are processes that can precipitate electrons. In cyclotron resonance electrons exchange energy and/or momentum with the waves, which can lead to pitch angle scattering of the electrons. When the scattering results in diffusion of electrons toward the atmospheric loss cone they are more likely to be lost to the atmosphere. The types of wave that undergo resonance interactions with radiation belt electrons are those in the VLF range, i.e., whistler mode waves such as chorus, plasmaspheric hiss, and in the ULF range, i.e., waves such as electromagnetic ion cyclotron (EMIC), Pc5. Background conditions also play a role in the efficiency of the wave-particle interactions with magnetic field strength and cold plasma density, as well as their gradients, being important [Schulz and Lanzerotti, 1974; Li et al., 2013].

Each wave mode has its own characteristic frequency spectrum, amplitude range, L -shell range, magnetic local time (MLT) range, and response to geomagnetic storm activity [e.g., Anderson et al., 1992; Usanova et al., 2012; Halford et al., 2016; Li et al., 2013; Agapitov et al., 2013]. These parameters ultimately define the characteristics of the electron precipitation, in particular the energy range involved, and the flux lost from the radiation belts. Knowledge of the electron precipitation characteristics driven by each wave type, and the circumstances under which they occur, is an important part of the understanding of the role of waves in the dynamics of the radiation belt electron populations.

However, precise measurements of the electron precipitation characteristics are not easy to make [e.g., *Rodger et al.*, 2010; *Nesse Tyssøy et al.*, 2016; *Crew et al.*, 2016]. There are three main techniques that are used: satellite detectors, high-altitude balloon-lofted platforms, and ground-based instrumentation. Low-altitude satellite detectors are able to make measurements of electron fluxes close to and inside the atmospheric bounce loss cone (BLC). However, at low altitudes the rapidly moving satellites only sample radiation belt fluxes for short periods (minutes) in each orbit, making the separation of spatial and temporal variations difficult, although twin or constellation satellite combinations can ameliorate this difficulty to some extent.

High-altitude balloon measurements can be used to measure energetic electron precipitation. Inverting the spectrum of emitted bremsstrahlung X-rays, which are received at altitudes of ~ 30 km, can provide information of the spectrum and flux of the incoming energetic electrons as they deposit the majority of the energy in the atmosphere at ~ 70 – 100 km. However, measurements are limited in spatial extent to the region near the balloon, data are available only while the balloons are aloft, and the L -shell sampling of the balloons is governed by the direction of the prevailing winds. The Balloon Array for Relativistic Radiation-belt Electron Losses (BARREL) southern hemisphere high-altitude campaigns associated with the NASA Van Allen Probes mission [*Mauk et al.*, 2012] were undertaken twice, initially for ~ 1.5 months starting in January 2013, and then again in January 2014. Each year ~ 20 balloons were launched with the expectation that several balloons would be aloft at any given time, and their locations would be at L shells that would be appropriate to detect electron precipitation from outer radiation belt processes [*Millan et al.*, 2013; *Woodger et al.*, 2015].

Several authors have analyzed BARREL X-ray spectra in order to provide insight into the precipitating electron energy spectra occurring during specific events. *Li et al.* [2014] studied an EMIC event at 03:00 UT on 17 January 2013 and calculated diffusion coefficients from a helium-band EMIC wave by using observed wave power and background conditions from GOES 13 and the Van Allen Probes. The simulated BARREL X-ray spectra best fit the observations when they were scaled down by a factor of 2.9. The inferred energy spectrum was peaked at ~ 1 MeV. *Woodger et al.* [2015] studied a relativistic electron precipitation event at 23:20 UT on 19 January 2013. A model of the scaled Magnetic Electron Ion Spectrometer (MagEIS) radiation belt electron spectrum close to the loss cone significantly overpredicted the expected BARREL X-ray flux from 600 to 1000 keV. In fact, the best fit to the BARREL X-ray flux spectrum was a 1350 keV mono-energetic electron spectrum. *Halford et al.* [2015] used BARREL observations to study a solar wind shock event and the resultant radiation-belt electron precipitation. Chorus wave amplitudes from Radiation Belt Storm Probes B (RBSP-B) were used to calculate the energy-dependent diffusion coefficients close to the bounce loss cone, which were shown to decrease by an order of magnitude for energies > 100 keV. This was reasonably consistent with the BARREL X-ray spectra observations of electron precipitation < 90 keV.

In these previous studies satellite measurements of electron fluxes close to the bounce loss cone were used to estimate the equivalent BARREL X-ray flux spectra. In the current study we investigate, for the first time, the technique of using the BARREL X-ray spectra to infer the equivalent effects on ground-based observing platforms, i.e., narrowband radio wave measurements and riometer absorption. We thus provide the first ground-based comparison of the energetic electron precipitation fluxes determined directly from BARREL X-ray observations.

Ground-based subionospheric VLF radio wave measurements, such as those observed by the Antarctic-Arctic Radiation-belt (Dynamic) Deposition-VLF Atmospheric Research Konsortium (AARDDVARK) network of instruments, can be used to determine the flux of electron precipitation through modeling the phase and amplitude perturbations that occur on great circle paths between VLF transmitters and receivers [*Clilverd et al.*, 2009; *Rodger et al.*, 2012]. The advantages of the technique come from good signal quality, continuous high time resolution measurements, and well-defined great circle paths. The regions where electron precipitation can be detected are typically large (hundreds of kilometers), with small-scale variations smoothed out by the integration of perturbation effects along the path. However, uncertainties in modeling electron precipitation data by using VLF subionospheric radio wave signals come in part from the difficulty in determining the fraction of the great circle path that is affected. A different technique relies on ground-based HF riometers to measure the opacity of the ionosphere. The absorption of the background cosmic noise at ~ 15 – 70 MHz can be used to infer the flux and spectrum of precipitating electrons [e.g., *Kero et al.*, 2014], potentially with high time resolution, although the measurement is usually limited to a relatively small viewing region close to overhead of the receiver site.

Recent studies have compared satellite electron flux observations of energetic electron precipitation with high-altitude balloon X-ray measurements. *Blum et al.* [2013] investigated two energetic electron precipitation bands by using the Colorado Student Space Weather Experiment (CSSWE) CubeSat. Enhancements in the combined trapped and precipitating flux of 0.58–3.8 MeV electrons were observed by the satellite detectors on 18–19 January 2013. Precipitation events with X-ray energies extending to >500 keV were concurrently seen by a BARREL balloon located in the Antarctic conjugate to the satellite. Estimates of the flux being precipitated indicated that at $L \sim 5$ up to 5% of the 0.58–3.8 MeV radiation belt electrons were lost during each event, suggesting that they could play an important role in radiation belt dynamics. In a follow-up study, *Blum et al.* [2015] associated the relativistic electron precipitation, from the same events, with duskside electromagnetic ion cyclotron (EMIC) waves observed by GOES 13 and ground-based magnetometers. The duskside EMIC waves were associated with nightside substorm injections following a solar wind pressure pulse. The observational evidence presented supported the earlier suggestion that EMIC waves could play a significant role in the loss of MeV electrons from the outer radiation belt [*Millan and Thorne, 2007; Li et al., 2014*].

In this study a detailed comparison of the energetic electron precipitation fluxes and spectra on 18–19 January 2013 is performed, using subionospheric radio wave data from the AARDDVARK network as well as riometer ground-based instruments and a BARREL high-altitude balloon. BARREL balloon observations are used to define the electron energy spectrum and fluxes involved in the precipitation events, the radio wave data to investigate the large and small-scale precipitation structures, and their evolution with time. To the best of our knowledge this is the first attempt to reconcile all of these different kinds of measurement techniques. The combination of all of these different instruments is highly important because it provides us with the possibility of extended spatial and temporal analyses as well as the spectral characteristics of the electron precipitation. However, the analysis requires the knowledge of how to interpret the different measurements together. Here we illustrate the more general description of the analysis procedure by undertaking the interpretation of two specific events, opening up a new opportunity for energetic and relativistic electron precipitation analyses.

2. Experimental Setup

The BARREL balloon 1C was at an altitude of ~ 36 km at the time of the events studied on 18–19 January. The BARREL balloons were equipped with spectrometers, detecting bremsstrahlung X-rays in the energy range from 20 keV to 10 MeV [*Millan et al., 2013*]. Using Monte Carlo simulations it is possible to convert the measured X-ray spectrum to an incident/precipitating electron energy spectrum [*Berger and Seltzer, 1972; Foat et al., 1998; Woodger et al., 2015*]. On 18–19 January 2013 BARREL 1C was at $L \sim 5$, south of the Weddell Sea, Antarctica, drifting slowly westward having been launched from Halley on 16 January. The location of the balloon was near-conjugate to the CSSWE CubeSat northern hemisphere passing through the $L \sim 5$ latitudinal contour when the precipitation events were detected.

To study the energetic electron precipitation fluxes into the atmosphere on 18–19 January 2013, narrowband subionospheric very low frequency/low-frequency radio wave data are used, spanning 20–40 kHz received at Halley, Antarctica ($75^{\circ}30'S$, $26^{\circ}54'W$, $L = 4.5$), and Ottawa, Canada ($45^{\circ}24'N$, $75^{\circ}33'W$, $L = 3.1$). These sites are part of the AARDDVARK network ([*Cliilverd et al., 2009*] for further information see the description of the array at www.physics.otago.ac.nz/space/AARDDVARK_homepage.htm). The transmitters studied have call signs NPM (21.4 kHz, $21^{\circ}26'N$, $158^{\circ}09'W$, $L = 1.2$) and NRK (37.5 kHz, geographic $63^{\circ}51'N$, $22^{\circ}28'W$, $L = 5.5$). Additional radio wave data were collected from two remote AARDDVARK field sites in the Antarctic, i.e., Fletcher Ice Dome (AA2, $76^{\circ}54'S$, $82^{\circ}36'W$, $L = 4.8$) and Pine Island Glacier (AA3, $75^{\circ}32'S$, $95^{\circ}33'W$, $L = 4.6$). Both receivers monitored the NPM transmitter in Hawaii, and together with the Halley AARDDVARK receiver, can be used to identify the location of electron precipitation along the NPM-Halley great circle path (see [*Cliilverd et al. 2013*] for more details). The remote field sites were removed in February 2014, at the end of the BARREL southern hemisphere campaigns.

The observations made by the CSSWE CubeSat are well documented by *Blum et al.* [2013]. The satellite was in an orbit with 65° inclination and 480×780 km altitude [*Li et al., 2013*]. The onboard instrument, the Relativistic Electron and Proton Telescope Integrated Little Experiment [*Schiller and Mahendrakumar, 2010*], consists of a single telescope with a stack of three operating solid state detectors. Based on the depth of

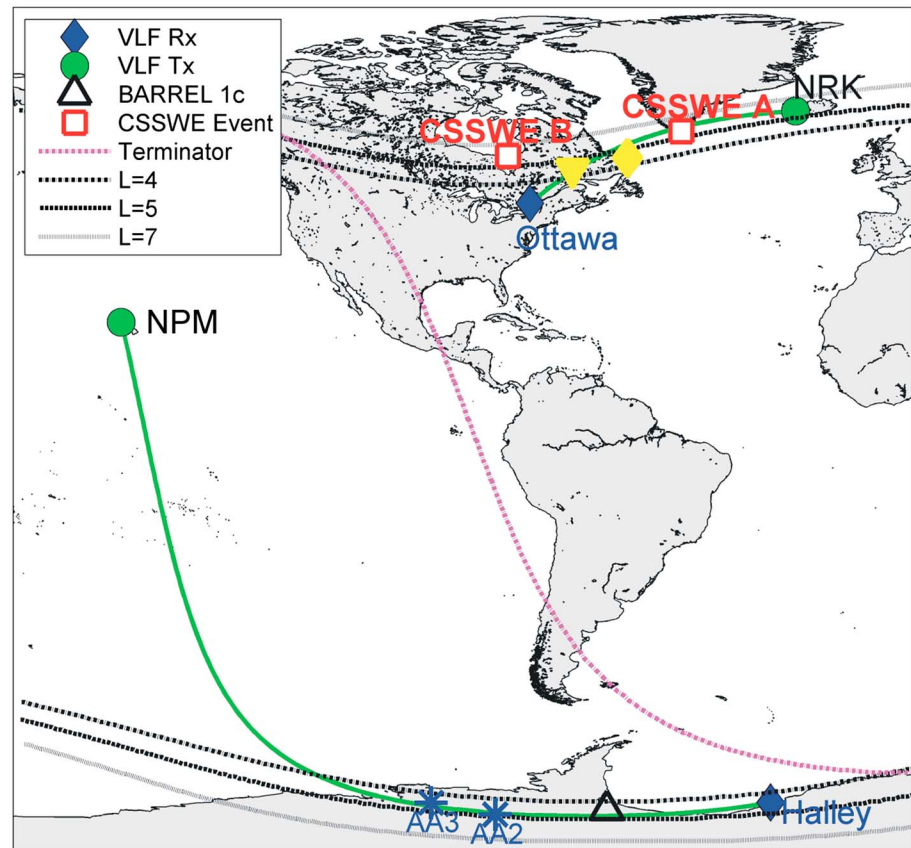


Figure 1. The location of the main subionospheric propagation paths analyzed in this study. The VLF transmitters are indicated by green circles and the AARDDVARK receiver sites by blue diamonds (permanent sites) and blue asterisks (temporary, solar powered sites). Also shown are the location of BARREL balloon 1C (triangle) and the two different event locations identified by the CSSWE CubeSat (events A and B, red squares). The conjugate locations of Halley and the BARREL balloon are shown by yellow diamond and triangle markers, respectively. The day-night terminator location at 24:00 UT on 18 January 2013 is indicated by the magenta dashed line, with daylight conditions existing to the west of the line.

penetration into the stack, and the energy deposited in each detector, the measurements are binned into three electron energy channels ($E_1 = 0.58\text{--}1.63$ MeV, $E_2 = 1.63\text{--}3.8$ MeV, and $E_3 \geq 3.8$ MeV). Due to the strong scattering of energetic electrons in the detector materials, some fraction of the electrons below 1.63 MeV will impact the second detector and trigger the second energy channel E_2 [e.g., Schiller *et al.*, 2014, Figure 3]. This is typically corrected for in the data processing by assuming a power law spectrum (see Li *et al.* [2013] for details). Additionally, with a field of view of 58° oriented orthogonally to the background magnetic field, the CubeSat measures a combination of both mirroring and precipitating electrons. In the time of interest two electron precipitation events were observed by CSSWE, one at 23:03 UT on 18 January 2013 (event A) and the other during the next pass of the same region, at about 00:38 UT on 19 January 2013 (event B). The events were detected in the northern hemisphere at $L \sim 5$. These details regarding the location and timing of the CSSWE observed events identified as A and B [Blum *et al.*, 2013] are used in order to provide context for the balloon and ground-based observations analyzed in this study.

Figure 1 shows the experimental setup during the 18–19 January 2013 events. In the southern hemisphere the BARREL 1C balloon (triangle) was drifting west of Halley, near the southern extremity of the Weddell Sea (79°S , 60°W , $L = 5.1$). The balloon was located west of Halley (diamond) but east of AA2 and AA3 (asterisks). IGRF L -shell contours for $L = 4$, 5, and 7 under quiet geomagnetic conditions are shown. The three AARDDVARK receivers all monitored NPM transmitting from Hawaii and were located close to, or on, the great circle path from NPM to Halley (green line) so that they could differentiate the precipitation occurring along that particular path. In the northern hemisphere the CSSWE satellite locations at the times of the 23:03 UT event (A) and 00:38 UT event (B) are shown by squares, with the NRK, Iceland, to Ottawa great circle

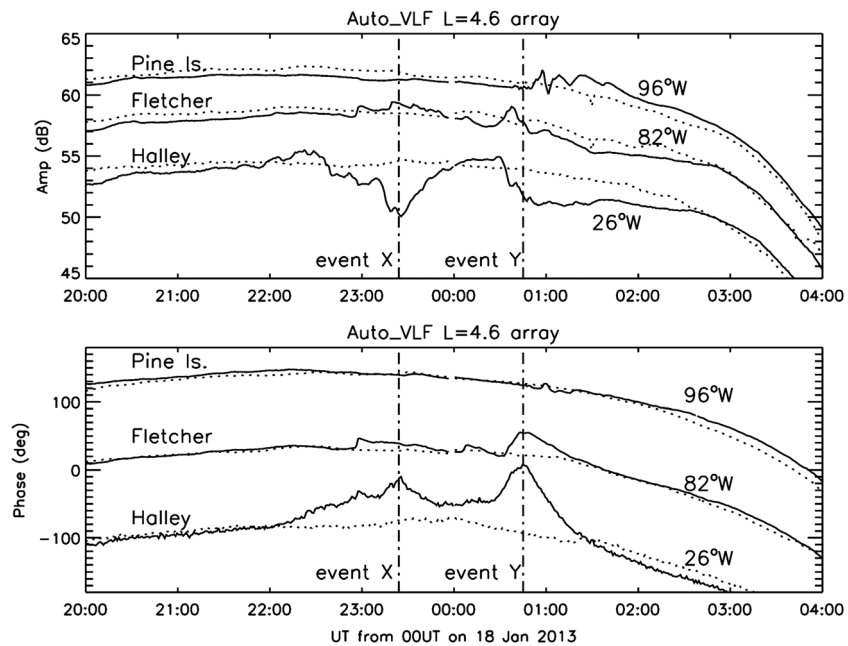


Figure 2. The variation of amplitude and phase of the NPM transmitter, Hawaii, observed at Pine Island Glacier, Fletcher Ice Dome, and Halley station in Antarctica. The actual phase and amplitude values have been offset such that the observations are organized with distance from the transmitter, where Pine Island is nearest and Halley is farthest. The dotted lines represent quiet day curves. The two vertical dashed lines indicate the times of peak phase perturbation observed at Halley and are identified as events X and Y.

subionospheric propagation path (green line) also indicated. The day-night terminator at 00:00 UT on 19 January 2013 is shown by the magenta dashed line and indicates that the measurements made in the northern hemisphere were made in darkness, while those in the southern hemisphere were in daylight conditions.

3. Results

Electron precipitation causes amplitude and phase perturbations of subionospheric radio waves by creating excess ionization below the altitude of the ionospheric *D* region [Rodger *et al.*, 2012]. The excess ionization lowers the effective reflection height and advances the phase at the receiver. Dependent on the position of the receiver within the interference fringes of the transmitted signal, the change in effective reflection height will produce increases or decreases in amplitude at the receiver [Barr *et al.*, 2000; Clilverd *et al.*, 2010; Clilverd *et al.*, 2015]. In Figure 2 the variation of the NPM amplitude (top) and phase (bottom) is shown from the three southern hemisphere AARDDVARK receivers located at $L \sim 4.5\text{--}4.8$. The nondisturbed variations of NPM phase and amplitude at each site are indicated by dotted lines. The vertical dashed lines identify the times of the peak phase perturbations observed at Halley and are labeled as events X and Y. The peak phase of the two precipitation events occurred at times that largely correspond to the CSSWE satellite observations of events A and B (e.g., 23:00–23:30 UT and 00:15–01:15 UT, respectively). For clarity we label the events in this study as X and Y as there is not necessarily a one-to-one comparison between the satellite events A and B and the ground-based events. The phase advance associated with event X starts shortly after 22:00 UT and shows a double-peaked structure, indicating that some precipitation was occurring on the Hawaii–Halley path from that time onward, lasting until $\sim 01:30$ UT. Although there is little evidence of any significant perturbation observed in the Pine Island data from further to the west, the Fletcher Ice Dome and Halley data show similar features for event Y, but event X is not observed at Fletcher.

In the northern hemisphere the electron precipitation events were observed on subionospheric great circle paths that passed close to the footprint of the CSSWE satellite when it observed events A and B. In Figure 1 the orientation of the NRK (Iceland)–Ottawa path is shown to be in close proximity to the location of CSSWE

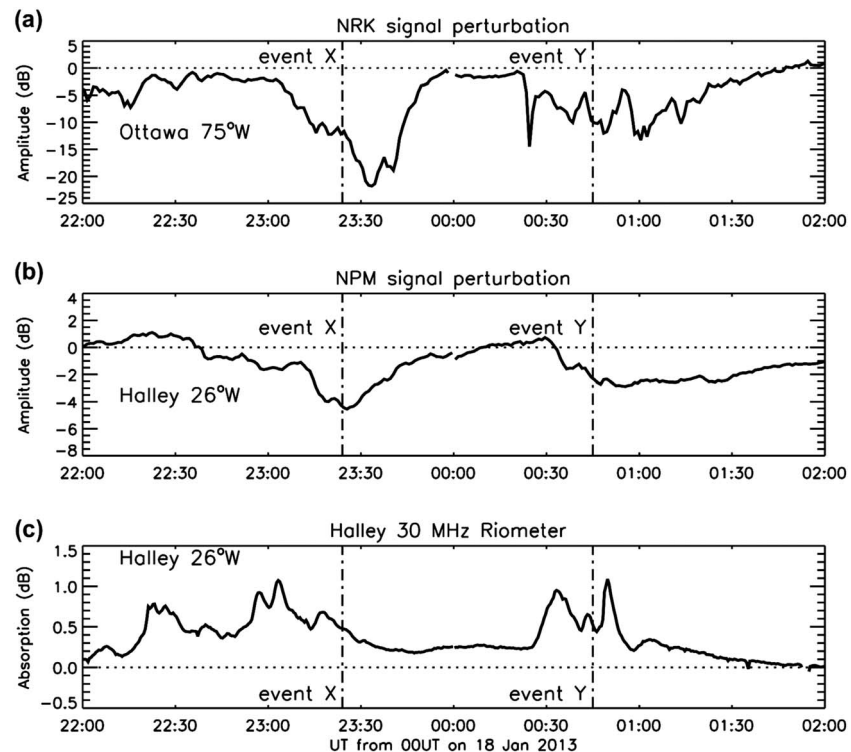


Figure 3. (a) Northern hemisphere observations: amplitude perturbations observed on the NRK transmitter (Iceland) received at Ottawa, Canada, from 22:00 UT 18 January 2013 to 02:00 UT 19 January 2013. (b) Southern hemisphere observations: amplitude perturbations observed on the NPM transmitter (Hawaii) received at Halley. (c) Riometer absorption at Halley. The geographical longitude of each instrument is given in the panel (see Figure 1 for the relative positions of the propagation paths and Halley). The vertical dashed lines represent the times of events X and Y.

magnetic field-line footprint during event A. Figure 3a shows the northern hemisphere NRK-Ottawa amplitude perturbations during the study period in 18–19 January 2013. As in previous figures, the times of events X and Y are plotted as vertical dashed lines. The NRK-Ottawa path also responds to both events. Figure 3b shows the southern hemisphere NPM-Halley amplitude perturbations. Figures 3a and 3b confirm that electron precipitation is occurring in both hemispheres and with similar temporal structure.

At the eastern edge of the study region it is possible to investigate the Halley riometer data (shown in Figure 3c). Absorption values are shown, determined from the single, 30 MHz, vertically pointing, wide-beam antenna. The timing of event Y (00:30–01:30 UT) is concurrent with enhanced riometer absorption of ~ 1 dB, which is consistent with the picture of a large precipitation patch seen at most sites (Halley, BARREL 1C, NPM-Halley, and NPM-Fletcher) at the same time with no discernible drift. However, event X (23:00–23:45 UT) does not show similarity in the timing of enhanced riometer absorption, which has an absorption peak ~ 13 min earlier at 23:00 UT. The timing of the riometer absorption peak is almost coincident with the published timing of event A seen by the CSSWE satellite, i.e., 23:03 UT [Blum *et al.*, 2013], when the satellite was close to the Halley conjugate longitude. One interpretation of the event X data is of a patch of precipitation moving westward, initially affecting Halley (26°W , $\text{MLT} = \text{UT} + 2.7$) and CSSWE before reaching BARREL 1C (60°W , $\text{MLT} = \text{UT} + 3.8$) about 13 min later, and then fading away before it could be detected westward of Fletcher Ice Dome ($>82^\circ\text{W}$). This westward propagation of event X is consistent with an ion drift with a period of 5–6 h for 10–100 keV proton energies associated with substorm injections [Clilverd *et al.*, 2015].

Only one other BARREL balloon showed a count-rate increase during the 3 h time period studied. The X-ray count rate observed on 1D (at about the same L shell as 1C but 2 h west in MLT) peaked weakly for a few minutes at 01:05 UT on 19 January 2013, consistent with the westward motion of event Y, covering ~ 2 h of MLT in ~ 20 min. Both the weak peak associated with event Y and the lack of any detectable event X by 1D are in agreement with the evolution of the precipitation patches inferred from Fletcher Ice Dome and Pine Island Glacier observations. Balloon 1G was located west of 1C, at the higher $L \sim 7$, and saw no precipitation

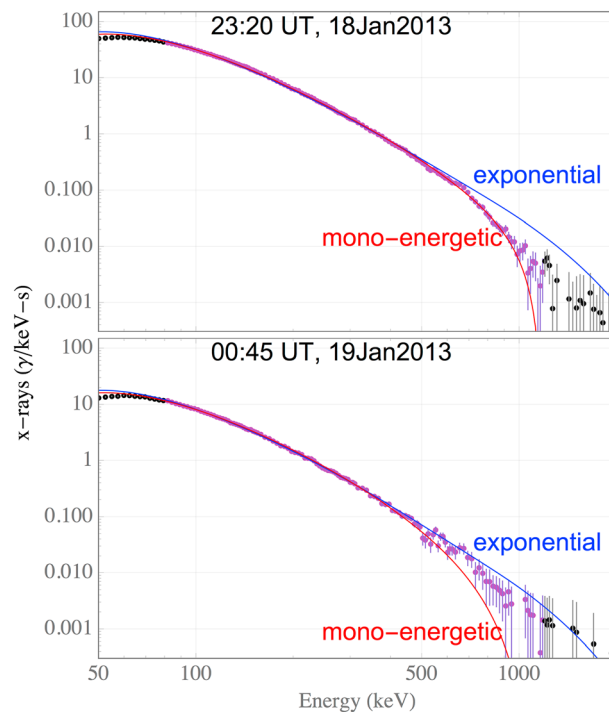


Figure 4. (top) BARREL background-subtracted 1C X-ray spectra for event X at 23:20 UT on 18 January 2013; the fits are shown for an exponential electron spectrum model with a characteristic e -folding of 440 keV (blue line) and a 1.14 MeV mono-energetic model (red line). The measurements are indicated by points with error bars, which show uncertainties propagated from the counting statistics. The black points do not contribute to the fitting, while the purple ones do. (bottom) Same format as Figure 4 (top) but for event Y at 00:45 UT on 19 January 2013, with an e -folding of 365 keV and 1.05 MeV mono-energetic fits.

to limited statistics at the highest energies of interest, a direct inversion of these data into electron spectra is difficult. In contrast, given a precipitating electron spectrum plus information about a detector, nearby materials, and the intervening atmosphere, one can calculate the resultant X-ray spectrum [Berger and Seltzer, 1972; Woodger *et al.*, 2015], and then compare it with the actual measurements. Hence, rather than inverting the X-ray observations to a unique electron spectrum, it is feasible to identify and reject electron spectrum models that are inconsistent with the observations or to select from candidate electron spectrum models one whose computed X-ray spectrum best matches the observed X-ray spectrum. For our analysis, the spectrum-matching procedure considers flux measurements in the 80–1200 keV energy range of each measured X-ray spectrum, and then explores parameter space to minimize the chi-square statistic. In Figure 4 the black points on the left-hand side of the panels were omitted due to systematic uncertainties in the BARREL response function at low energies [Woodger *et al.*, 2015]. The black points on the right-hand side of the panels were omitted because above 1200 keV, measurements become indistinguishable from the background model for many of the selected spectra. The 1200 keV cutoff value is a compromise that permits the same analysis to be applied to each spectrum, while including the energy range of significant flux increase. Success in this endeavor requires one to begin with a reasonable model for the electron spectrum and to evaluate whether or not the resulting X-ray spectrum, from each best fit electron model, adequately matches the corresponding observed X-ray spectrum. The BARREL response used here has been determined by using GEANT 3 Monte Carlo simulations as described in more detail in Woodger *et al.* [2015].

Two models for electron spectra were considered: the first is exponential and the second is mono-energetic. The peaked character of the mono-energetic energy spectrum is representative of the sort of electron precipitation spectra potentially driven by EMIC waves, using insight gained from the analysis of Van Allen Probes electron spectra, and fits to similar BARREL observations [Millan *et al.*, 2002; Li *et al.*, 2014; Woodger *et al.*, 2015; Halford *et al.*, 2015]. Figure 4 presents an example of model evaluation. Two panels show the X-ray energy

associated with either event X or event Y. Balloons 1I and 1K were in the polar cap at much higher L and so have nothing to contribute to these radiation belt studies.

4. BARREL Spectral Information

Our objective is to quantitatively compare ionospheric changes, obtained from ground-based measurements, with precipitating electron spectra, as inferred from BARREL balloon 1C X-ray measurements. The X-ray spectra are modeled by two different electron precipitation spectra, one representing the type of process that precipitates the ambient trapped population (exponential) and a second that represents an energy-selective mechanism (mono-energetic). This section describes the analysis, its evaluation, and implications for processes responsible for the electron precipitation.

The data for this analysis are a series of time-integrated (320 s) X-ray spectra, each modified by subtracting away a background spectrum. Due

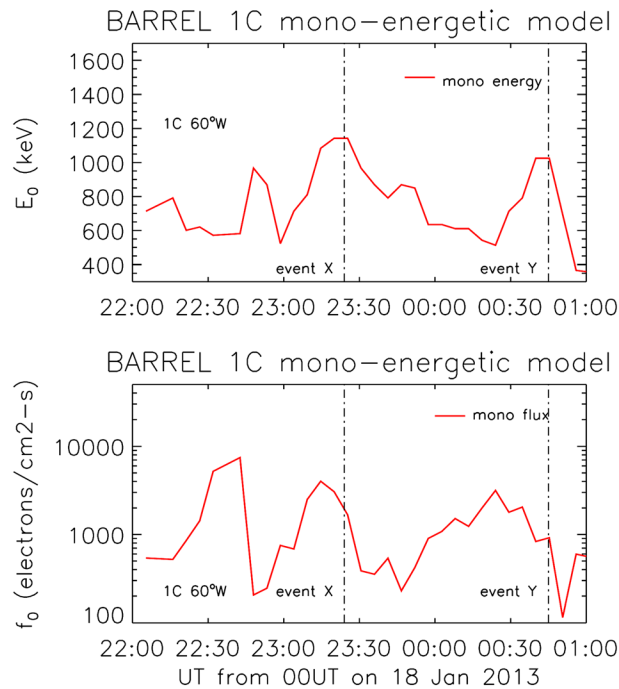


Figure 5. (top) The variation of the energy (E_0) for the mono-energetic model (red line) from 22:00 UT on 18 January to 01:12 UT on 19 January. The times of events X and Y are indicated by vertical dashed lines. (bottom) The flux of electrons (f_0) for the mono-energetic model.

around the time indicated in the panels. Overall it is found that both of the models provide qualitatively good agreement with the BARREL X-ray spectra from 80 to 500 keV. However, at X-ray energies above 500 keV, the exponential model overpredicts the X-ray fluxes, while the mono-energetic model shows good agreement with the BARREL spectrum, particularly for the event at 23:20 UT. As a result of this finding no further calculations are undertaken in this study with the exponential spectrum model. The mono-energy model provides a better match with the X-ray fluxes up to 1 MeV. This result suggests that the loss mechanism involved is not a process that precipitates the ambient trapped population but is energy-selective. This is consistent with the spectral characteristics of precipitation associated with EMIC waves determined by *Li et al.* [2014] and *Woodger et al.* [2015].

The fits for a mono-energetic electron spectrum model ($f(E) = f_0 \delta(E - E_0)$, with $f(E)$ as the electron differential flux at energy E and two modeling parameters f_0 as a scale factor and E_0 as the characteristic energy) are shown in Figure 5, where the panels display the characteristic energy and scaling factor, respectively, covering the interval 22:00 UT on 18 January to 01:12 UT on 19 January. As in the previous figures, the dashed vertical lines indicate the times of events X and Y. At the times of events X and Y, peaks in the characteristic energy parameter are seen, with values reaching 1–1.2 MeV. Peak flux values of $\sim 4 \times 10^3 \text{ el cm}^{-2} \text{ s}^{-1}$ were seen during the events. These values are similar to those reported by *Woodger et al.* [2015] during a similar precipitation event later on 19 January 2013, i.e., a mono-energetic 1.35 MeV beam with peak fluxes of $2.6 \times 10^3 \text{ el cm}^{-2} \text{ s}^{-1}$. Both the fluxes in this present study and those of *Woodger et al.* [2015] are approximately an order of magnitude lower than those reported by *Blum et al.* [2013] in the analysis of the CSSWE observations. This could be due to uncertainty in removing the trapped flux population from the CSSWE measurements or the separation in measurement locations. The uncertainty estimates in this study were calculated for the exponential and mono-energetic models by resampling from Poisson distributions of each observed channel, changing the contributing energy range, and by changing the time interval of the 320 s averages. In each case the uncertainties in energy were $<5\%$ and the uncertainties in flux were $<20\%$.

During the two events, the scale parameter slowly decreases. Although a decrease in electron flux when X-ray production and ionization are increasing may seem puzzling, the increasing energy parameter must also be considered. Both ionization and X-ray flux depend on the total electron energy deposition, which is the

spectrum observed during event X (23:20 UT on 18 January 2013) and event Y (00:45 UT on 19 January 2013). The BARREL slow spectrum product is shown, evaluating 256 energy bins. The data are from the background-subtracted BARREL slow spectrum product, where a background spectrum was constructed from observations during the quiet interval of 20:30–21:30 UT on 18 January 2013. Measurements are indicated by points with error bars, which show uncertainties propagated from the counting statistics. As discussed above, the black points do not contribute to the fitting, while the purple ones, which are inside the 80–1200 keV range, do.

The two curves show X-ray spectra derived from the best fit exponential (solid blue) and mono-energy (red) precipitating electron spectrum models. The best fit is made to the data taken over the 320 s sample

product of the scale and energy parameters. By definition, the mono-energetic model requires that only a narrow electron energy subpopulation can precipitate. The results from this electron model are consistent with a process that selects varying electron fluxes and energies to precipitate, with higher energy-MeV electrons precipitating at the event times. The mono-energetic spectral model suggests that peak precipitation fluxes occur at 1.0–1.2 MeV during the events studied here and that the loss mechanism involved is energy-selective. We note here that additional analysis of the BARREL spectra, undertaken by varying the X-ray upper energy range between 800 and 2000 keV, made no significant changes to the best fit parameters. In order to check the methodology of this study, we have also undertaken an analysis of the RBSP data by using the technique outlined in Woodger *et al.* [2015]. Initially, the RBSP *MagEIS* electron spectrum was determined at the time of the two events studied, at $L = 5$, for pitch angles close to the loss cone, finding the fluxes to be reasonably represented by an exponential distribution. Using the BARREL analysis software package (BDAS software) the applied *MagEIS* electron spectrum significantly overpredicted the observed BARREL X-ray flux in 600–1000 keV range for events X and Y, as was also determined in our analysis shown in Figure 4. However, the same exponential spectrum with a lower energy cutoff at 1 MeV was able to reproduce the BARREL X-ray flux observations closely for both events. This check confirms that the methodology used in this study is reasonable and that a peaked energy spectrum of ~ 1 MeV is required to reproduce the observed BARREL X-ray spectrum rather than the ambient exponential spectrum observed by the RBSP *MagEIS* instrument.

5. Comparison With Ground-Based Observations

In this section the BARREL 1C mono-energetic electron precipitation spectra and fluxes are used to calculate the magnitude of the perturbations seen by the Halley ground-based instruments, i.e., the AARDDVARK receiver and the riometer. The methods of calculating the perturbation magnitude for these instruments are given in detail in Rodger *et al.* [2012] and Simon Wedlund *et al.* [2014]. The vertical charge density profile is given by the BARREL analysis, with horizontally homogeneous patch structure assumed. Figure 6a shows the observed perturbations of the northern-hemisphere NRK-Ottawa amplitude (black line) in comparison to the calculated perturbations using the mono-energetic fits to the BARREL 1C X-ray data (red line). Here we preferentially investigate the amplitude variations rather than the phase because of large uncertainties in some of the modeled and observed phase results during the comparison period. Although the observed perturbations are large (~ 15 dB) the modeling does reproduce the maximum perturbation levels of the precipitation events well suggesting that the path is sensitive to electron precipitation and that the BARREL fluxes are a reasonable description of the precipitation fluxes in the opposite hemisphere. In order to model the variation of the perturbation amplitude during event X it was necessary to apply a westward propagating patch of ionization to the NRK-Ottawa path. The patch covered 1000 km of the path, starting close to the transmitter and moving westward at ~ 30 km/min or a drift period of ~ 11 h. This is consistent with the westward drift identified from the combined riometer and BARREL observations in the southern hemisphere as discussed in section 3. The different drift periods (5 and 11 h) estimated for the same patch, but viewed from opposite ends of the field line, are indicative of the uncertainties in estimating the speeds using longitudinally aligned, long-path AARDDVARK observations. The comparison of the modeling results to the observations for event Y is consistent with the precipitation patch being large, covering most of the NRK-Ottawa propagation path.

Figure 6b shows the same format as Figure 6a but for the southern hemisphere NPM-Halley path. Good agreement is observed for the mono-energetic spectral model. These results suggest that the BARREL fluxes are representative of the precipitation conditions in the southern hemisphere close to the balloon and also in the conjugate northern hemisphere region near the CSSWE CubeSat. Southern hemisphere precipitation fluxes close to Atlantic longitudes are typically larger than those in the northern hemisphere because of the influence of the South Atlantic magnetic anomaly [e.g., Andersson *et al.*, 2014], although the results presented here suggest that the interhemispheric differences are not significant during these particular events—potentially indicating that strong diffusion into the BLC is taking place [Kennel and Petschek, 1966].

In order to allow for an apparent propagation time delay of the peak effect from BARREL 1C to the peak response of the NPM-Halley path, a time shift of 6 min has been applied to the AARDDVARK data to align it with the peak perturbations calculated from the BARREL spectra, i.e., for both events X and Y. The 6 min timing difference between the BARREL observations and the AARDDVARK NPM-Halley observations is consistent with the idea of a moving precipitation patch and allows for the separation distance of the BARREL

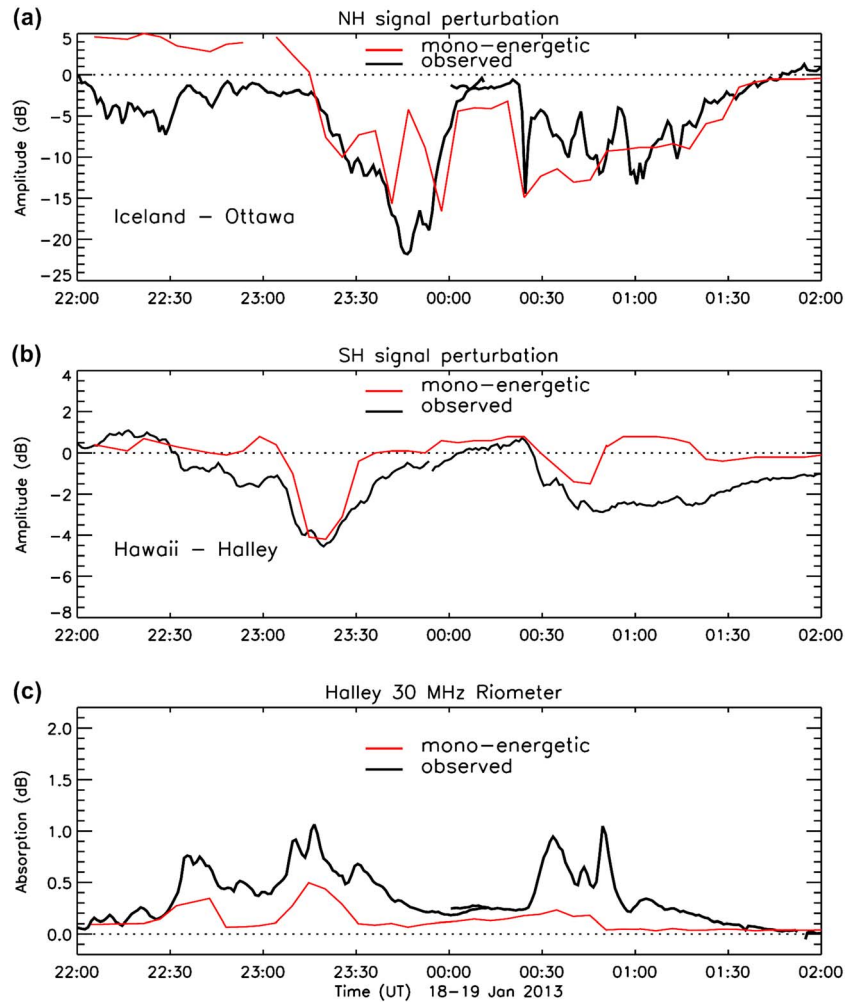


Figure 6. (a) Northern hemisphere: the observed perturbations of NRK-Ottawa amplitude (black line) in comparison with the calculated perturbations using the mono-energetic fits to the BARREL 1C X-ray data (red line). (b) As in Figure 6a but for the southern hemisphere observed perturbations of NPM-Halley. (c) As in Figure 6a but for the observed riometer absorption at Halley. Time shifts have been added to this plot to line up the data sets taking into account the movement of the precipitation patches and can be seen as an overlap of the black lines at 24:00 UT—see text for more details.

balloon from the region of highest sensitivity of the NPM-Halley path, to the west of the balloon location. However, the region of highest sensitivity of the NPM-Halley path is not precisely known, and no estimate of drift period can be made from these observations.

Figure 6c shows the variation of observed 30 MHz riometer absorption at Halley. In this panel the observed riometer absorption data from 18 January (event X) have been shifted by 13 min in order to allow for the separation distance from the riometer at Halley to the BARREL balloon and the apparent propagation time of the precipitation region to move westward from the riometer to the BARREL 1C location. Halley and BARREL 1C were separated by ~1 h of MLT at the time, so a drift time between the two of 13 min is equivalent to a drift period of 5–6 h. The observed riometer absorption on 19 January (event Y) has not been time shifted because the precipitation patch appears to be large enough to be seen simultaneously at Halley and the BARREL balloon locations. The results of the 13 min shift of the riometer data can be seen as a short overlap between the black absorption traces at 24:00 UT.

In the absorption data the time variations of the absorption are well matched, suggesting that the offset of 13 min between the Halley riometer observations and those of BARREL 1C is reasonable for event X and indicating a precipitation patch moving westward. Similarly, the well-matched temporal variations between the Halley riometer and the BARREL 1C spectra models suggest that event Y occurs at about the same time at

both locations, suggesting a larger precipitation patch than for event X. It is important to remember that the time shift of 13 min between the riometer and BARREL 1C observations of event X means that temporal changes in precipitation fluxes could have occurred.

The amplitude variations shown in Figures 6a and 6b indicate some agreement between the spectral model and the observations, both in the northern hemisphere and in the southern hemisphere. In the southern hemisphere the perturbation values for event X were modeled by using a small, 26° wide in longitude, patch centered on the longitude of BARREL 1C (60°W). The perturbation values for event Y were modeled by imposing a patch which was 70° wide, also centered on the BARREL 1C location. In the northern hemisphere the patch size for event X was ~18° wide, while for event Y it was the majority of the path, i.e., ~50° wide. Larger patch dimensions in the southern hemisphere compared with those in the northern hemisphere are entirely consistent with the configuration of the geomagnetic field around the American longitudes, where there are substantial differences in the geographic longitudes of conjugate points (see the discussion in *Clilverd et al.* [1991]). It is therefore preferable to express the precipitation patch longitude dimensions in MLT, where event X covers ~1.5 h in MLT and event Y covers ~3.5 h in MLT. The change from small patch to large patch in the modeling occurred at 00:30 UT. A small patch size for event X and a large patch size for event Y are consistent with the observations from all of the instruments described in section 3. The width of the nightside EMIC-induced precipitation patches of 1.5–3.5 h in MLT found in this study supports the findings of *Clilverd et al.* [2015] who determined the width of an earlier EMIC-induced electron precipitation patch to be only a few degrees across in latitude but ~50° wide in longitude (i.e., ~3 h in MLT). Together these findings suggest duskside EMIC precipitation patches to be narrow in latitude but much wider in longitude. A more statistical analysis of EMIC-induced precipitation patch dimensions is currently being undertaken.

In the southern hemisphere the modeled perturbation amplitudes recover to near-zero after event Y much more quickly than is observed (see Figure 6b), suggesting that electron precipitation continues to affect the NPM-Halley subionospheric propagation path even after the precipitation event has ended at BARREL 1C and that the precipitation patch has moved westward of BARREL 1C. The recovery of the perturbation associated with event Y in the northern hemisphere (see Figure 6a) is consistent with the BARREL balloon conjugate location being close to the Ottawa receiver longitude, and thus, when the fluxes diminish at BARREL, they also diminish on the NRK-Ottawa path. Again, this is consistent with a westward moving patch, and with the expected drift direction for ions, and thus potentially an EMIC-driven source. This conclusion is supported by *Blum et al.* [2015] who identified substorm injected particles that may have led to EMIC wave growth associated with this event.

The overall analysis of Figure 6 suggests that it is possible to use the BARREL 1C X-ray fluxes to provide an accurate estimate of the perturbations observed on the AARDDVARK subionospheric radio wave amplitude signals and the riometer. The comparison with the riometer observations did show that there were some temporal differences with longitude that had to be taken into account, particularly for event X, and an analysis of the AARDDVARK data showed that precipitation patch size needs to be taken into account.

6. Summary

A previous analysis of two electron precipitation events observed on 18/19 January 2013 [*Blum et al.*, 2013, 2015] has suggested that potentially significant fluxes of relativistic electrons are lost from the outer radiation belt as a result of EMIC-driven wave-particle resonance interactions. The current study, using a novel, powerful combination of simultaneous balloon and ground-based observations in an analysis of the same precipitation events, reveals the following:

1. BARREL X-ray fluxes at the peak of two precipitation events can be well modeled by a mono-energetic spectrum but not by a simple exponential spectrum. These observations suggest that the loss mechanism involved is energy-selective rather than one that simply precipitates the ambient trapped radiation belt population. The analysis of the events shows that they have peaked electron precipitation fluxes at energies of ~1.0–1.2 MeV. However, improved instrumentation is required to unambiguously resolve the spectral form.
2. The BARREL-based ~1.0–1.2 MeV mono-energetic electron precipitation fluxes have been used for the first time to successfully reproduce the observed amplitude perturbations on the AARDDVARK subionospheric radio wave signals and the Halley 30 MHz riometer.

- The ground-based observations provide indications of the precipitation patch size and the propagation of the patches through the observation region. The precipitation patches are found to be drifting westward at speeds that are consistent with 10–1000 keV ion drift periods of 5–11 h at $L \sim 5$. The duskside patches exhibit different dimensions, with the first event covering ~ 18 – 26° in longitude and the second 50– 70° (1.5–3.5 h in MLT). The westward drift, ~ 1 MeV peaked energy spectra, and the longitudinal dimensions support the hypothesis that the electron precipitation events were generated by EMIC waves.

In this study we have shown the potential of the added ground-based observations, when combined with balloon and satellite measurements. The ground-based observations have provided temporal and spatial contexts for the single-point measurement platforms, identifying electron precipitation event characteristics and behavior that would have been difficult to resolve without their inclusion.

Acknowledgments

Data for this paper are available at the British Antarctic Survey Polar Data Centre (<http://psddb.nerc-bas.ac.uk/data/access/>). M.A.C. and N.C. would like to acknowledge the important contributions from Nick Alford and Tom Stroud, particularly for their skill and assistance in building and deploying the autonomous AARDDVARK systems. The authors would like to thank the Natural Environmental Research Council/British Antarctic Survey and the South African National Antarctic Program for their support and collaboration during the BARREL balloon campaigns. The research leading to these results has received funding from the Natural Environmental Research Council under the Antarctic Funding Initiative (AFI/11/22). C.J.R. was supported by the New Zealand Marsden Fund. M.M. was supported (through Dartmouth College) on the NASA grant NNX08AM58G. This work was supported in part by the CSSWE funding grant NSF AGSW 0940277 as well as the JHU/APL contract 922613 (RBSP-EFW). The Dartmouth College portion of this work was supported by NASA grant NNX08AM58G. This research was supported by the International Space Science Institute's International Teams program project no. 329.

References

- Agapitov, O., A. Artemyev, V. Krasnoselskikh, Y. V. Khotyaintsev, D. Mourenas, H. Breuillard, M. Balikhin, and G. Rolland (2013), Statistics of whistler mode waves in the outer radiation belt: Cluster STAFF-SA measurements, *J. Geophys. Res. Space Physics*, *118*, 3407–3420, doi:10.1002/jgra.50312.
- Anderson, B. J., R. E. Erlandson, and L. J. Zanetti (1992), A statistical study of Pc 1–2 magnetic pulsations in the equatorial magnetosphere: 1. Equatorial occurrence distributions, *J. Geophys. Res.*, *97*, 3075–3088, doi:10.1029/91JA02706.
- Andersson, M. E., P. T. Verronen, C. J. Rodger, M. A. Clilverd, and S. Wang (2014), Longitudinal hotspots in the mesospheric OH variations due to energetic electron precipitation, *Atmos. Chem. Phys.*, *14*, 1095–1105, doi:10.5194/acp-14-1095-2014.
- Barr, R., D. L. Jones, and C. J. Rodger (2000), ELF and VLF radio waves, *J. Atmos. Sol. Terr. Phys.*, *62*(17–18), 1689–1718, doi:10.1016/S1364-6826(00)00121-8.
- Berger, M. J., and S. M. Seltzer (1972), Bremsstrahlung in the atmosphere, *J. Atmos. Sol. Terr. Phys.*, *34*, 85–108, doi:10.1016/0021-9169(72)90006-2.
- Blum, L. W., Q. Schiller, X. Li, R. Millan, A. Halford, and L. Woodger (2013), New conjunctive CubeSat and balloon measurements to quantify rapid energetic electron precipitation, *Geophys. Res. Lett.*, *40*, 5833–5837, doi:10.1002/2013GL058546.
- Blum, L. W., et al. (2015), Observations of coincident EMIC wave activity and duskside energetic electron precipitation on 18–19 January 2013, *Geophys. Res. Lett.*, *42*, 5727–5735, doi:10.1002/2015GL065245.
- Clilverd, M. A., A. J. Smith, and N. R. Thomson (1991), The annual variation in quiet time plasmaspheric electron density, determined from whistler mode group delays, *Planet. Space Sci.*, *39*, 1059–1067, doi:10.1016/0032-0633(91)90113-O.
- Clilverd, M. A., C. J. Rodger, R. J. Gamble, T. Ulich, T. Raita, A. Seppälä, J. C. Green, N. R. Thomson, J.-A. Sauvaud, and M. Parrot (2010), Ground-based estimates of outer radiation belt energetic electron precipitation fluxes into the atmosphere, *J. Geophys. Res.*, *115*, A12304, doi:10.1029/2010JA015638.
- Clilverd, M. A., N. Cobbett, C. J. Rodger, J. B. Brundell, M. Denton, D. Hartley, J. Rodriguez, D. Danskin, T. Raita, and E. L. Spanswick (2013), Energetic electron precipitation characteristics observed from Antarctica during a flux dropout event, *J. Geophys. Res. Space Physics*, *118*, 6921–6935, doi:10.1002/2013JA019067.
- Clilverd, M. A., R. Duthie, R. Hardman, A. T. Hendry, C. J. Rodger, T. Raita, M. Engebretson, M. R. Lessard, D. Danskin, and D. K. Milling (2015), Electron precipitation from EMIC waves: A case study from 31 May 2013, *J. Geophys. Res. Space Physics*, *120*, 3618–3631, doi:10.1002/2015JA021090.
- Clilverd, M. A., et al. (2009), Remote sensing space weather events: The AARDDVARK network, *Space Weather*, *7*, S04001, doi:10.1029/2008SW000412.
- Crew, A. B., et al. (2016), First multipoint in situ observations of electron microbursts: Initial results from the NSF FIREBIRD II mission, *J. Geophys. Res. Space Physics*, *121*, 5272–5283, doi:10.1002/2016JA022485.
- Foat, J. E., R. P. Lin, D. M. Smith, F. Fenrich, R. Millan, I. Roth, K. R. Lorentzen, M. P. McCarthy, G. K. Parks, and J. P. Treilhou (1998), First detection of a terrestrial MeV X-ray burst, *Geophys. Res. Lett.*, *25*, 4109–4112, doi:10.1029/1998GL900134.
- Halford, A. J., S. L. McGregor, M. K. Hudson, R. M. Millan, and B. T. Kress (2016), BARREL observations of a solar energetic electron and solar energetic proton event, *J. Geophys. Res. Space Physics*, *121*, 4205–4216, doi:10.1002/2016JA022462.
- Halford, A. J., et al. (2015), BARREL observations of an ICME-shock impact with the magnetosphere and the resultant radiation belt electron loss, *J. Geophys. Res. Space Physics*, *120*, 2557–2570, doi:10.1002/2014JA020873.
- Horne, R. B., M. M. Lam, and J. C. Green (2009), Energetic electron precipitation from the outer radiation belt during geomagnetic storms, *Geophys. Res. Lett.*, *36*, L19104, doi:10.1029/2009GL040236.
- Kennel, C. F., and H. F. Petschek (1966), Limit on stably trapped particle fluxes, *J. Geophys. Res.*, *71*, 1–28, doi:10.1029/JZ071i001p00001.
- Kero, A., J. Vierinen, D. McKay-Bukowski, C.-F. Enell, M. Sinor, L. Roininen, and Y. Ogawa (2014), Ionospheric electron density profiles inverted from a spectral riometer measurement, *Geophys. Res. Lett.*, *41*, 5370–5375, doi:10.1002/2014GL060986.
- Li, X., et al. (2013), First results from CSSWE CubeSat: Characteristics of relativistic electrons in the near-Earth environment during the October 2012 magnetic storms, *J. Geophys. Res. Space Physics*, *118*, 6489–6499, doi:10.1002/2013JA019342.
- Li, Z., et al. (2014), Investigation of EMIC wave scattering as the cause for the BARREL 17 January 2013 relativistic electron precipitation event: A quantitative comparison of simulation with observations, *Geophys. Res. Lett.*, *41*, 8722–8729, doi:10.1002/2014GL062273.
- Mauk, B. H., N. J. Fox, S. G. Kanekal, R. L. Kessel, D. G. Sibeck, and A. Ukhorskiy (2012), Science objectives and rationale for the Radiation Belt Storm Probes mission, *Space Sci. Rev.*, *179*(1–4), 3–27, doi:10.1007/s11214-012-9908-y.
- Millan, R. M., and R. M. Thorne (2007), Review of radiation belt relativistic electron loss, *J. Atmos. Sol. Terr. Phys.*, *69*, 362–377, doi:10.1016/j.jastp.2006.06.019.
- Millan, R. M., R. P. Lin, D. M. Smith, K. R. Lorentzen, and M. P. McCarthy (2002), X-ray observations of MeV electron precipitation with a balloon-borne germanium spectrometer, *Geophys. Res. Lett.*, *29*(24), 2194, doi:10.1029/2002GL015922.
- Millan, R. M., et al. (2013), The balloon array for RBSP relativistic electron losses (BARREL), *Space Sci. Rev.*, *179*, 503–530, doi:10.1007/s11214-013-9971-z.

- Nesse Tyssøy, H., M. I. Sandanger, L.-K. G. Ødegaard, J. Stadsnes, A. Aasnes, and A. E. Zawedde (2016), Energetic electron precipitation into the middle atmosphere—Constructing the loss cone fluxes from MEPED POES, *J. Geophys. Res. Space Physics*, *121*, 5693–5707, doi:10.1002/2016JA022752.
- Rodger, C. J., M. A. Clilverd, J. C. Green, and M. M. Lam (2010), Use of POES SEM-2 observations to examine radiation belt dynamics and energetic electron precipitation into the atmosphere, *J. Geophys. Res.*, *115*, A04202, doi:10.1029/2008JA014023.
- Rodger, C. J., M. A. Clilverd, A. J. Kavanagh, C. E. J. Watt, P. T. Verronen, and T. Raita (2012), Contrasting the responses of three different ground-based instruments to energetic electron precipitation, *Radio Sci.*, *47*, RS2021, doi:10.1029/2011RS004971.
- Schiller, Q., and A. Mahendrakumar (2010), REPTile: A miniaturized detector for a CubeSat mission to measure relativistic particles in near-Earth space, Small Satellite Conference, AIAA/USU.
- Schiller, Q., D. Gerhardt, L. W. Blum, X. Li, and S. Palo (2014), Design and scientific return of a miniaturized particle telescope onboard the Colorado Student Space Weather Experiment (CSSWE) CubeSat, *Aero. Conf., IEEE*, doi:10.1109/AERO.2014.6836372.
- Schulz, M., and L. J. Lanzerotti (1974), *Particle Diffusion in the Radiation Belts, Physics and Chemistry in Space*, vol. 7, Springer, Berlin, Heidelberg, New York.
- Simon Wedlund, M., M. A. Clilverd, C. J. Rodger, K. Cresswell-Moorcock, N. Cobbett, P. Breen, D. Danskin, E. Spanswick, and J. V. Rodriguez (2014), A statistical approach to determining energetic outer radiation belt electron precipitation fluxes, *J. Geophys. Res. Space Physics*, *119*, 3961–3978, doi:10.1002/2013JA019715.
- Thorne, R. M. (2010), Radiation belt dynamics: The importance of wave-particle interactions, *Geophys. Res. Lett.*, *37*, L22107, doi:10.1029/2010GL044990.
- Usanova, M. E., I. R. Mann, J. Bortnik, L. Shao, and V. Angelopoulos (2012), THEMIS observations of electromagnetic ion cyclotron wave occurrence: Dependence on AE, SYMH, and solar wind dynamic pressure, *J. Geophys. Res.*, *117*, A10218, doi:10.1029/2012JA018049.
- Woodger, L. A., A. J. Halford, R. M. Millan, M. P. McCarthy, D. M. Smith, G. S. Bowers, J. G. Sample, B. R. Anderson, and X. Liang (2015), A summary of the BARREL campaigns: Technique for studying electron precipitation, *J. Geophys. Res. Space Physics*, *120*, 4922–4935, doi:10.1002/2014JA020874.